# Electronic and Structural Differences between Wurtzite and Zinc Blende InAs Nanowire Surfaces: Experiment and Theory

Martin Hjort,[†] Sebastian Lehmann,[†] Johan Knutsson,[†] Alexei A. Zakharov,[‡] Yaojun A. Du,[§] Sung Sakong,[§] Rainer Timm,[†] Gustav Nylund,[†] Edvin Lundgren,[†] Peter Kratzer,[§] Kimberly A. Dick,[†,||] and Anders Mikkelsen*,[†]

[†]Department of Physics and The Nanometer Structure Consortium, Lund University, P.O. Box 118, 221 00 Lund, Sweden, [‡]MAX IV-Laboratory, Lund University, P.O. Box 118, 221 00 Lund, Sweden, [§]Fakultät für Physik and Center for Nanointegration (CENIDE), Universität Duisburg-Essen, Lotharstrasse 1, 470 48 Duisburg, Germany, and [||]Centre for Analysis and Synthesis, Lund University, P.O. Box 124, 221 00 Lund, Sweden

ABSTRACT We determine the detailed differences in geometry and band structure between wurtzite (Wz) and zinc blende (Zb) InAs nanowire (NW) surfaces using scanning tunneling microscopy/spectroscopy and photoemission electron microscopy. By establishing unreconstructed and defect-free surface facets for both Wz and Zb, we can reliably measure differences between valence and conduction band edges, the local vacuum levels, and geometric relaxations to the few-millielectronvolt and few-picometer levels, respectively. Surface and bulk density functional theory calculations agree well with the experimental findings and are used to interpret the results, allowing us to obtain information on both surface and bulk electronic structure. We can thus exclude several previously proposed explanations for the observed differences in conductivity of Wz-Zb NW devices. Instead, fundamental structural differences at the atomic scale and nanoscale that we observed between NW surface facets can explain the device behavior.
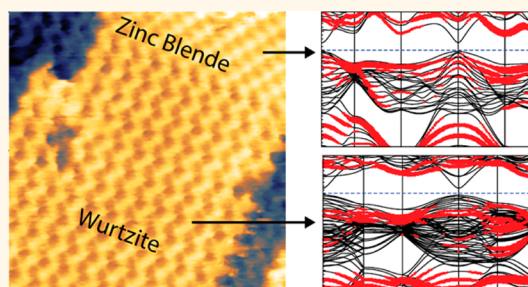
KEYWORDS: STM · InAs nanowire · surface · STS · PEEM · wurtzite

Many 1D nanoscale objects experience significant variations in their crystal structure along the growth direction. Such variations can influence the electronic properties of the structures and degrade device performance. As a result, there are considerable efforts going into controlling effects related to crystal structure variations and understanding their influence on nanodevice performance.[1,2] One system that is particularly interesting in this respect is the InAs nanowire (NW) system. It is especially favorable in that ohmic electrical connections are easily established and InAs NWs can be reliably synthesized using a wide variety of growth methods. In addition they are considered as components for important applications as photodetectors[3] and low-power electronics[4–6] and are highly useful for fundamental studies of,

for example, the existence of Majorana fermions.[7] All the efforts have resulted in a very thorough experimental knowledge of the device performance of InAs NWs. Nonetheless, while it has been established experimentally that variations in crystal structure influence electronic properties of NWs,[2,8,9] the origin of these electronic effects is less clear. Several mechanisms have been proposed, including a staggered band alignment, polarization charges in the interface between the crystallites, differences in doping, surface oxide formation, and adsorbates on the surface (e.g., from processing). The main reason for this discrepancy is that all these different effects can potentially lead to similar influences on, for example, conductivity, and without solid input parameters for modeling it is very difficult to pinpoint the relevance of each effect. In

the present study we remove the surface defect pinning effects and measure down to the atomic scale. As a result, we can directly determine the unperturbed bulk band gap and alignment and put strict limits on crystal structure induced polarization charges, making it possible to single out the most relevant effects in real functioning devices. Recently, it has become possible to not only grow defect-free InAs NWs[10] but also to tailor the crystal structure between the zinc blende (Zb) structure and the wurtzite (Wz) structure with atomically sharp interfaces within single NWs.[11] This allows for the new design of devices and for careful studies of crystal structures and structural transitions not possible in the bulk, where Zb is the thermodynamically stable structure. With the availability of highly controlled NWs, it becomes possible to directly compare structural parameters for different III−V structures using advanced imaging techniques. To do this, we need to develop our experimental tools that have successfully allowed for such studies on 2D surfaces to the situation of high aspect ratio 1D objects. Scanning tunneling microscopy/spectroscopy (STM/S) is one central technique that has contributed greatly to the development of III−V research.[12] STM enables the study of surface reconstructions and direct measurements of the bulk band gap and Fermi level position, if unreconstructed surfaces like the (110) Zb surface can be found. Recently, STM/S was developed to allow for studies of III−V NWs,[13−17] where removal of the native oxide and the large height differences of tens to hundreds of nanometers owing to the NW geometry pose significant technical challenges. Two other surface-sensitive microscopy methods, low-energy and photoemission electron microscopy (LEEM/PEEM), have possibilities for structural characterization by spatially resolved low-energy electron diffraction (μLEED) and chemical and electronic characterization using PEEM.[17−19] Both methods are performed within the same microscope and offer vast possibilities for detailed surface characterization. In combination with STM/S, the band structure in the vicinity of the Fermi level as well as the local vacuum level position can be extracted.[20] The position of the local vacuum level, and thus the work function, is important to characterize since it will determine electron transport into the vacuum or across contacts. With the high degree of control of NW crystal structure, facet morphology, and defect formation during oxide removal in the present study, we can obtain InAs NW surfaces that are not dominated by defect states as in previous studies and are thus accessible to a well-defined study using our full suite of experimental techniques. This is particularly interesting since InAs surfaces uniquely among the III−Vs show the existence of 2D electron gases (2DEGs) due to the presence of surface defects.[21,22]

Density functional theory (DFT) calculations have proven to be valuable to predict electronic and geometric properties of NWs.[16,23] However, comparisons between theory and experiment, and even between experiments, have so far been unreliable since results are usually significantly affected by different setups. Our crystal-structure-engineered NWs, where different segments have been analyzed under identical conditions, allow for an elegant test of DFT for these surfaces. Furthermore, the calculations enable interpretation of the experimental results to distinguish between bulk and surface contributions to the density of states (DOS) and disentangle structural and geometric effects. Determining the surface DOS and the surface Fermi level position (and the reliability of theory to predict these) is crucial for NWs since they experience a high surface-to-bulk ratio and surface properties can govern both optical and electronic properties. In our setup we perform a direct comparison between theory and experiment for both structural and electronic properties.

In this letter we describe the surface analysis of InAs NWs with well-defined axial stacking of alternating Wz and Zb segments displaying low-index side facets of mainly {110}-, {10$\bar{1}$0}-, and {11$\bar{2}$0}- type. Using STM/S, we have analyzed the surface morphology, the atomic-scale structure, and the electronic properties in the vicinity of the Fermi level. Using PEEM, we have been able to probe the local vacuum level position outside the different segments, and by combining the two methods, it has allowed us to determine the valence band maximum, the conduction band minimum, and the local vacuum level position for all facets and compare these to theoretical calculations. These fundamentally important parameters are relevant not only for our cleaned NWs; as they represent the case of no perturbation due to surface defects, they are the starting point for any discussion of the influence of the native oxide or any other film that might cover the surface of the NWs. Indeed in discussions found below, we use these values as the basic point of reference for understanding the influence of the surface oxide.

RESULTS AND DISCUSSION

In Figure 1, we present models and scanning electron micrographs of the grown NW structures. From the SEM images it is apparent that the side facets are very smooth and without extended defect segments, as the latter often can be identified by the formation of uneven sidewalls.[11,27]

The overall morphology of the NWs was investigated using STM. In Figure 2a, an interface between a {110}-terminated Zb segment and a {11$\bar{2}$0}-terminated Wz segment from the lower part of a NW is shown. The {110}-type facet is recognized by its large, flat, terraces with zigzag edges that result from an incomplete overgrowth of the underlying twin-plane superlattice.[28] The {11$\bar{2}$0} part was seen to have well-defined edges but with one-monolayer-high terraces
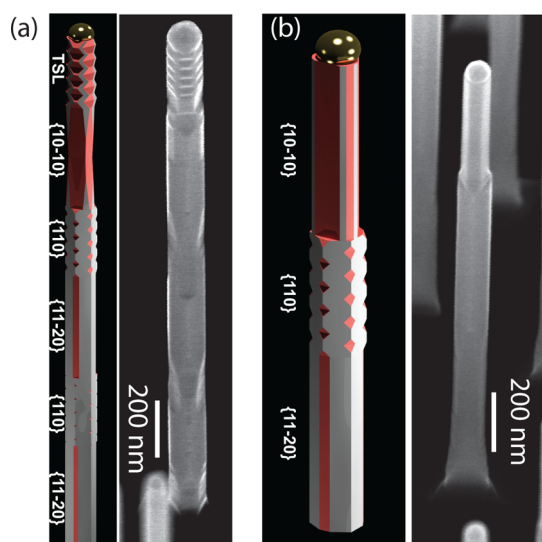
Figure 1. (a) Model and 30° tilted view scanning electron micrograph of the STM sample. (b) Model and 30° tilted view scanning electron micrograph of the LEEM/PEEM sample. The red color in the models denotes facets originating from Au-assisted vapor—liquid—solid-grown InAs ($\{10\bar{1}0\}$- and $\{111\}$-/$\{\bar{1}\bar{1}\bar{1}\}$-type facets), whereas the gray color denotes vapor—solid-overgrown InAs facets ($\{110\}$- and $\{11-20\}$-type) as described in ref 11.

Figure 2. STM results from a Wz—Zb InAs NW. (a) Overview image of a $\{11\bar{2}0\}$—$\{110\}$-type Wz—Zb interface on a NW. $U_{sample} = -1.0$ V, $I_t = 50$ pA. (b) Micrograph depicting As atoms on part of a rotationally twinned $\{110\}$ facet. $U_{sample} = -2.2$ V, $I_t = 100$ pA. (c) Atomic arrangement on the $\{11\bar{2}0\}$ facet. $U_{sample} = -2.3$ V, $I_t = 160$ pA. (d) Atomically sharp interface between $\{110\}$ and $\{11\bar{2}0\}$ facets. $U_{sample} = -2.5$ V, $I_t = 100$ pA. (e) $\{10\bar{1}0\}$ facet showing its characteristic appearance. $U_{sample} = -1.7$ V, $I_t = 80$ pA. (f) Red dots depict the placement of top layer As atoms at the $\{10\bar{1}0\}$ facet. $U_{sample} = -1.2$ V, $I_t = 80$ pA. (g) Profile along the dotted yellow line in (c) showing an outward relaxation at the Zb segment. Dashed green line marks the epitaxial junction. Dashed red lines mark the apparent tip height difference between the Wz and Zb surface. Red dots mark the positions of the topmost As atoms at the different surface facets. The NW growth direction, $[\bar{1}\bar{1}\bar{1}]/[000\bar{1}]$, is indicated in the images.

extending from the Wz—Zb interface along the NW growth direction; see Figure 2a,d. The $\{10\bar{1}0\}$ facet was similarly seen to exhibit a very smooth appearance with only occasional steps and low defect concentration as seen in Figure 2e. The top part of the NWs was terminated by alternating polar $\{111\}$- and $\{\bar{1}\bar{1}\bar{1}\}$-type facets; these facets were rough or reconstructed, as will be discussed in detail elsewhere.[28] We conclude that all nonpolar surfaces observed here were found to be smooth even after native oxide formation and native oxide removal, indicating a gentle deoxidation procedure, very similar to what we observed for GaAs NWs.[15]

In Figure 2b, a filled-state, atomically resolved image of the topmost As atoms at the $\{110\}$-type facet is depicted. The $\{110\}$ facet displays an unreconstructed surface with rows of atoms extending at a 35.4° angle to the NW growth direction, as has been reported previously.[14,16] The $\{110\}$ facet shows rotational twins, Figure 2b, every 20—30 nm, reminiscent of the direction of the overgrown twin plane superlattice. No differences in the atomic appearance (except for the twinning) were observed when comparing the $\{110\}$ NW facet and $\{110\}$ facets obtained by cleaving (001)-oriented bulk wafers. [Cleaved $\{110\}$ facets were studied both directly after cleavage in UHV and after oxidation and subsequent atomic hydrogen cleaning. No changes in the atomic appearance were observed.] The $\{11\bar{2}0\}$ facets display As atoms in a zigzag configuration, indicating a clean and unreconstructed surface.[14,16] The $\{10\bar{1}0\}$ facet, found at a 30° angle to the $\{11\bar{2}0\}$ facet (rotated along the NW growth axis),
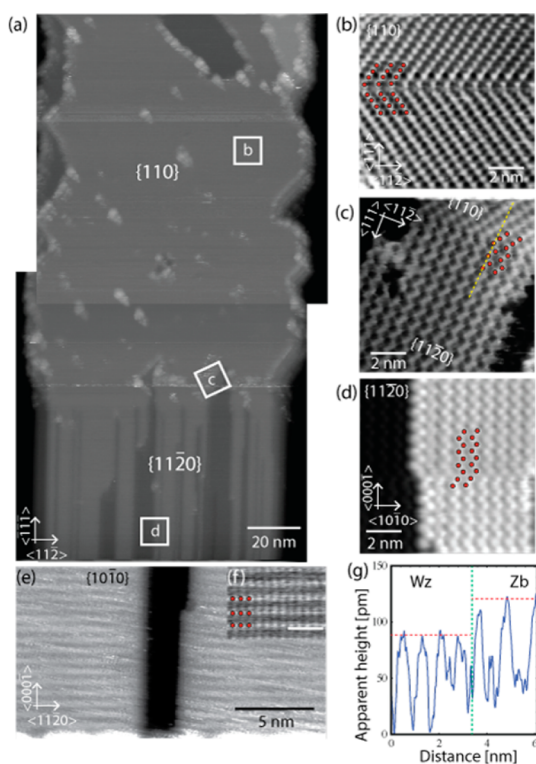
is similar to the other low-index facets, found to be unreconstructed (Figure 2f). This agrees well with our *ab initio* calculations (both this and previous work[16]) that also reveal the (1×1) surfaces to be the most stable for all three facets. The Wz—Zb interface as investigated at the $\{11\bar{2}0\}$—$\{110\}$ transition was found to be atomically sharp and without any steps obscuring the interface (Figure 2c), making it ideal for Wz—Zb interface studies. By measuring the *z*-piezo displacement of the STM tip scanning across the interface, we detect an outward relaxation of the Zb surface by 30 pm, as depicted in the profile in Figure 2g. This is consistent with the direction of a geometric relaxation of 10 pm found in our theoretical calculations. More importantly, we observe no indication of any charge accumulation at this interface. Previously it has been suggested that polarization charges could build up at the interface between the Wz and the Zb crystal
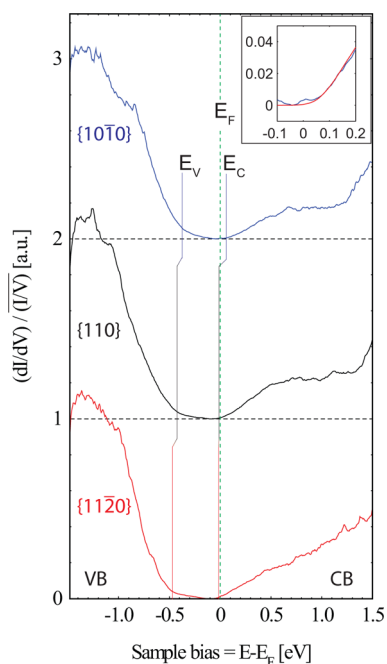
Figure 3. STS $(dI/dV)/\overline{(I/V)} - V$ plots depicting the LDOS as obtained at neighboring {110} and {11$\overline{2}$0} facets and at a {10$\overline{1}$0} facet. Ten to 15 individual spectra obtained at each facet were averaged to generate the final spectrum. Tunneling from valence and into conduction band states is marked VB and CB, respectively. The valence (E_V) and conduction band edges (E_C) are marked by the vertical lines. The Fermi level, E_F, is marked by the dashed green line. Inset shows the fitted band edge (red) for the {10$\overline{1}$0} conduction band edge. Details about band edge extraction can be found in the text.

structures.[9,29] Charging effects for example at surface steps are clearly observed in STM and appear upward or downward bending toward the charged interface.[30,31] No such effects are observed even when varying bias voltages, which indicates that the existence of such polarization charges to any relevant amount is highly unlikely.

After resolving the overall morphology as well as the atomic-scale structure of all the nonpolar, low-index facets we turned to Scanning Tunneling Spectroscopy (STS) for mapping the electronic structure around the Fermi level.

In Figure 3 we present STS data that are proportional to the local density of states (LDOS), obtained from neighboring {110} and {11$\overline{2}$0} facets as well as from a {10$\overline{1}$0} facet obtained separately. At negative sample bias, electrons associated with tunneling from filled valence band (VB) states are detected. Between approximately −0.5 and 0 V, the band gap with no or a very low amount of states can be seen. At positive sample bias electrons associated with tunneling into empty conduction band (CB) states are measured. The Fermi level, located at 0 V sample bias, is positioned close to the CB edge, as expected for nominally undoped InAs NWs, which have been reported to exhibit n-type conductivity.[2] Our previous measurements on InAs NWs[16] showed no signs of a band gap

region, which was attributed to step- and defect-induced states. The band gap energies measured here therefore indicate that we have achieved a clean and well-defined system, similar to what we observed for GaAs NWs.[15] The main reasons for the qualitatively improved results are better defined NWs with excellent crystal structure control and improved control in the native oxide removal step. In order to obtain a quantitative value for the experimentally determined band gap, we fit the band onsets. Following ref 32 we assume a linear increase in the LDOS close to the band edges and take temperature into account *via* Gaussian broadening (see inset of Figure 3). The obtained band gaps are larger than what has been reported previously for both Wz and Zb InAs. This is expected, as we will have tip-induced band bending (TIBB). The large diameter (∼100 nm) of our NWs rules out quantization effects (which was observed for small-diameter Si NWs[33]) as an explanation for the increased band gap. TIBB is an effect where some of the applied bias drops in the sample itself instead of in the vacuum region, resulting in enlarged observed band gaps.[34,35] The TIBB can be modeled for a hyperbolically shaped probe tip in the vicinity of a semiconductor using a 3D Poisson solver.[32,36,37] During acquisition of STS data at the neighboring {110} and {11$\overline{2}$0} facets the tip quality remained unchanged. It is therefore possible to fit the {110} data to the well-known band gap of 0.354 eV and use the same tip settings for the {11$\overline{2}$0} facet to deduce its properties. The uncorrected values are stated in the Supporting Information. From the modeling we find that the {110} spectrum can be fitted using reasonable assumptions: a tip with a 10 nm curvature and a 1 nm microtip, a 1 nm tip−sample distance, a contact potential (tip−sample work function difference) of −0.4 eV, a carrier concentration of 2×10^{17} cm^{-3}, a conduction band effective mass of $0.0635m_0$, heavy and light hole effective masses of $0.41m_0$ and $0.026m_0$, respectively. Using the same tip and sample parameters, the {11$\overline{2}$0} facet was found to have a 36 meV larger band gap.

The observed band gap difference compares favorably to results of DFT calculations. It is in good agreement with our HSE06 calculations that yield a 58 meV larger band gap for Wz InAs. It also fits well with LDA results by Murayama *et al.*, who proposed a Wz band gap 40 meV larger than the corresponding Zb.[38] It is smaller than the 70 meV larger band gap proposed by Belabbes *et al.*[39] on the basis of the so-called LDA+1/2 calculations including spin−orbit coupling. Experimentally, a photocurrent spectroscopy study of In-As$_{1-x}$P$_x$ NWs extrapolated to pure InAs gave a Wz InAs band gap 120 meV larger than Zb,[40] significantly larger than what we observed, but that study includes more assumptions in the analysis.

For the STS data obtained at the {10$\overline{1}$0} facet, the tip geometry is unknown, as this facet had to be

accessed on a different NW and tip changes cannot be ruled out. So while we present the band gap values for the {10$\bar{1}$0}-type facet, it is important to note that the values are more uncertain than for the {11$\bar{2}$0}-type facet. Still, assuming the same tip geometry as for the {11$\bar{2}$0} and the {110} facets, we retrieve a TIBB-corrected band gap 20 meV smaller than what was found for the other Wz facet, which already indicates some differences in the tip configuration of these measurements.

Analyzing the band alignment, we note that our calculations as well as several other studies have reported on a type-II staggered band offset in between Wz and Zb InAs.[38,39,41] Our theoretical modeling proposes VB offsets of 62 meV for small segments and 127 meV for larger segments (with Zb at more negative values). Experimentally, it was observed that the conduction band edges measured at the {110} and the {11$\bar{2}$0} facets were aligned (both before and after TIBB correction). Given the reliability of the theoretical calculations in predicting band gap differences, this is best explained by additional effects not included in the theoretical calculations and most probably due to the fact that the InAs NWs are inherently n-type, which could pin both materials and thus mask the band alignment of the pure materials.[42,43] Thus, we can conclude that the fundamental band alignment will not be present due to the n-type defects in the material.

Turning to the shape of the STS spectra, we note that at the VB side the obtained STS data resemble each other to a large degree with a VB edge around −0.5 V and similar STS structure at $V_t < -0.5$ V. At the CB side an onset at 0 V can be seen for all facets as well as comparable initial increase in differential conductivity; clear differences do however occur at $V_t > 0.5$ V. Due to the similar experimental conditions, the {110} and the {11$\bar{2}$0} facets are particularly suitable for a comparison of experiment and theory.

First, we need to address the question of to what extent the STS spectra represent the bulk DOS or the surface LDOS. In Figure 4, the LDA band structure for a {11$\bar{2}$0}-type, a {10−10}-type, and a {110}-type facet is presented. It is found that the LDOS of the surface As and In atoms (whose orbital weights are indicated by the red symbols) lies outside the principal band gap. Thus, one would expect that the STS spectra are dominated by the bulk DOS, similar to what we found for GaAs NW surfaces.[15] At higher energies, a surface band due to In dangling bond orbitals becomes visible in part of the Brillouin zone. This is especially pronounced for the {10$\bar{1}$0} facet, which also displays the smallest surface band gap. In Figure 5a, the bulk DOS of the two polytypes as obtained from HSE calculations aligned at the conduction band bottom to match the experimental data is shown. In agreement with experiment, the valence band DOS is almost indistinguishable for Zb and Wz, while clear differences are seen in
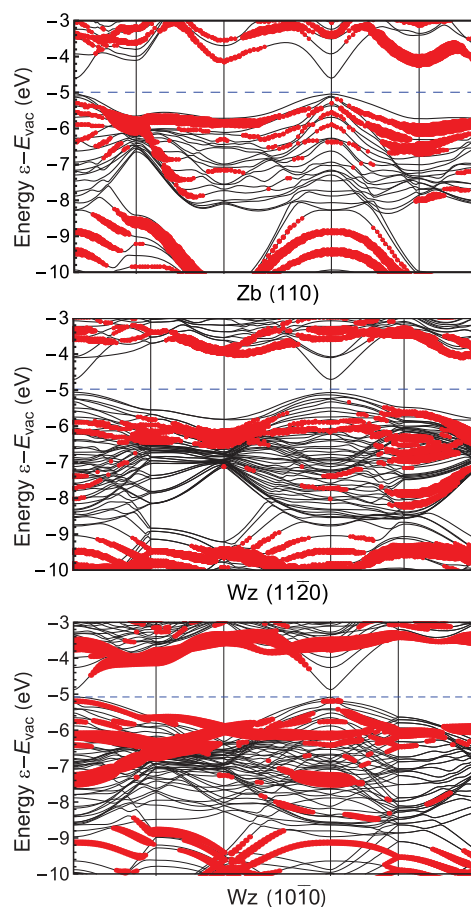

Figure 4. Band structure along the path Γ−X′−M−Γ−X−M for the Zb{110}-, the Wz{11$\bar{2}$0}-, and {10$\bar{1}$0}-type facets, respectively, as obtained from LDA slab calculations. Red points mark contributions from the surface bilayer (surface In and As atoms).

the conduction band. In both polytypes, the conduction band minimum (CBM) is formed by a band of Γ_7 symmetry. The calculated DOS of Zb displays a sharp rise at about 1.2 eV above the CBM, which corresponds to the L-valley conduction band, as has been noticed previously for bulk samples.[44] The CB DOS of Wz shows a gentler rise already at somewhat lower energies, which reflects the second lowest CB of Γ_8 symmetry.

Somewhat surprisingly, the STS measurement from the {10$\bar{1}$0} facet (see Figure 3) resembles the {110} facet more than the {11$\bar{2}$0} facet. As also indicated by the theoretical calculations, this is consistent with a stronger contribution of the surface DOS (see Figure 5b) to the tunneling current in the case of the {10$\bar{1}$0} facet, which would result in different STS spectra despite both surfaces having Wz structure. The general agreement between bulk theory calculations and experiment is good close to the band edges. Further away from the edges, surface-related states are needed in order to explain the experimental data. Importantly, we note that the integrated DOS is quite similar for the Wz and Zb structures; thus any electronic effects due to differences in the total density of states can also be excluded.
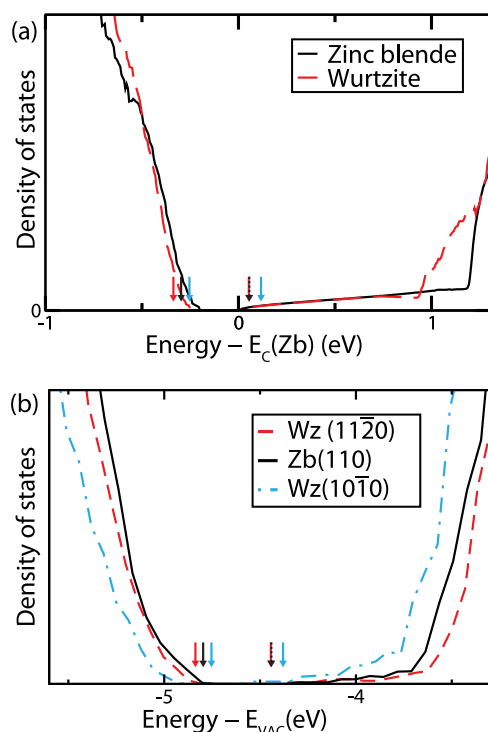
Figure 5. Density of states from HSE calculations (a) of bulk Wz and Zb, aligned at E_C, and (b) of the surface As and In atoms of Zb and Wz slabs. The arrows mark experimentally obtained valence and conduction band onsets for the $\{11\bar{2}0\}$ facet (red), $\{110\}$ facet (black), and $\{10\bar{1}0\}$ facet (blue).
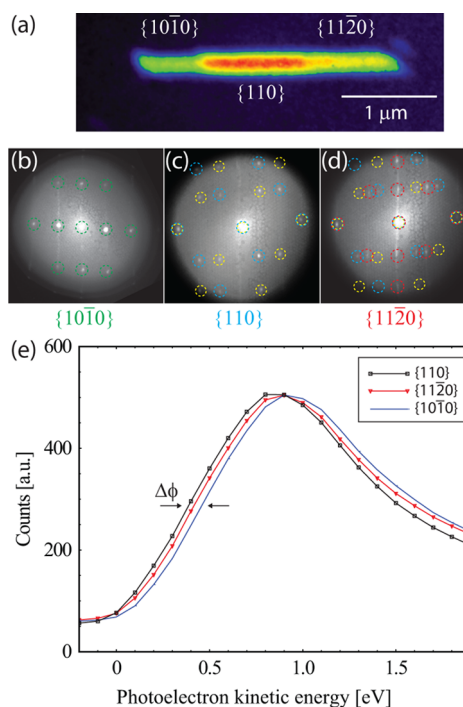

Figure 6. (a) PEEM image obtained using photoelectrons with 0.40 eV kinetic energy after excitation with 70 eV photons. The emission intensity is highest at the $\{110\}$ segment followed by the $\{11\bar{2}0\}$ and $\{10\bar{1}0\}$. μLEED pattern obtained from (b) $\{10\bar{1}0\}$ part showing (1×1) symmetry; (c) $\{110\}$ part showing two (1×1) domains rotated 71° with respect to each other colored in yellow and blue, respectively; (d) $\{11\bar{2}0\}$ part showing not only the (1×1) $\{11\bar{2}0\}$ pattern but also LEED spots from the two $\{110\}$ domains. All μLEED patterns were compiled by merging LEED patterns obtained using 15–30 eV electron energy. The streaks seen in the patterns arise from moving spots from side facets not normal to the incoming electron beam (i.e., inclined sides of the NW). (e) Number of photoelectrons as a function of the photoelectron kinetic energy for the three facets. The difference at the linear parts of the SE onset, $\Delta\phi$, is the difference in local vacuum level. The intensity has been normalized at maximum intensity position; photon energy used was 70 eV. An energy window of 0.5 eV was used for the PEEM images.

Another important variable is the position of the local vacuum level, which is a fundamental parameter of the surface indicating the barrier for electron emission. To measure this quantity, we performed surface-sensitive electron microscopy on the NWs. Using PEEM, the NWs were excited with synchrotron X-rays and an image was formed using photoelectrons with selected kinetic energy, Figure 6a. The NWs were found to have three segments emitting photoelectrons with varying intensity. The facet type of each segment was confirmed using μLEED, in which a 400 nm diameter aperture was inserted to selectively illuminate one NW segment at a time, Figure 6b–d. At the middle part a pattern consisting of two (1×1) $\{110\}$ domains rotated by 71° was recorded, colored yellow and blue in Figure 6c, corresponding to the two rotational domains found in STM rotated ±35.4° from the NW growth axis. At the rightmost (bottom) part of the NW a (1×1) $\{11\bar{2}0\}$ pattern was recorded, colored red in Figure 6d, but spots arising from the neighboring $\{110\}$ facet were also detected due to a slightly misplaced aperture. The $\{10\bar{1}0\}$ facet is inherently rotated by 30° around the NW growth direction and can therefore not give rise to stationary LEED spots if the $\{110\}$-type facet is oriented normally to the incoming electron beam. Instead, the top part of a NW lying close to where the $\{10\bar{1}0\}$-type facet was oriented perpendicularly to the electron beam was analyzed, and

a (1×1) $\{10\bar{1}0\}$ pattern was recorded, Figure 6b. The unreconstructed nature of all facets found in STM was thus corroborated using μLEED. We note that even at 200 eV electron kinetic energy clear μLEED patterns were obtained from the NWs, thus showing the general feasibility for future I(V) LEED measurements and therefore quantitative determination of the NW crystal surface structure.[45] In addition such spectra will be sensitive to changes in the atomic configuration of the unit cell and can thus also be used qualitatively to observe even small changes in the unit cell.

In order to map out the local vacuum level position, secondary electron X-ray photoemission electron microscopy (SE XPEEM) images were recorded close to the onset of secondary electron (SE) emission, and the intensity of each segment was plotted as a function of photoelectron kinetic energy. The shape of the SE peak, Figure 6e, is similar in all cases, but a notable shift

TABLE 1. TIBB-Corrected Valence (E_V) and Conduction (E_C) Band Edges with Respect to the Fermi Level as Well as Vacuum Level (E_{VAC}) Relative to {110} for the Different Facets[a]

	{110} [eV]	{11$\bar{2}$0} [eV]	{10$\bar{1}$0} [eV]
E_V: experiment	−0.297	−0.336	−0.254
E_V: theory	−0.291	−0.229	−0.229
E_C: experiment	0.0564	0.0538	0.117
E_C: theory	0	0.120	0.120
E_{VAC} relative to {110}: experiment	0	0.03	0.08
E_{VAC} relative to {110}: theory	0	0.048	0.108

[a] The theoretical values are calculated as obtained using the 62 meV valence band offset between Zb and Wz obtained from the superlattice (bulk) calculations, and ionization energies from the slab (surface) calculations.

of the curves along the photoelectron kinetic energy axis can be seen. In PEEM measurements, the sample is floating on high negative potential (−20 kV), whereas the detector is grounded. All photoelectrons emitted from the sample (within the acceptance angle of the microscope) can therefore be detected. The onset of SE emission will thus represent the lowest kinetic energy a photoelectron can have when escaping the sample.[17,18,20,46] Assuming an aligned Fermi level in the NW and measuring the onset difference at the linear part[17,47] yields the vacuum level difference for the segments. We find the lowest vacuum level potential for {110} followed by a 30 meV higher vacuum level for its Wz counterpart, {11$\bar{2}$0}, and an 80 meV higher vacuum level for {10$\bar{1}$0} (compared to {110}). These parameters agree well with theoretical calculations, as seen in Table 1.

In Table 1, we summarize our results regarding the band edges as determined by our combined approach and notice that it is partly agreeing well. For the {110} facet a band gap of about 350 meV could be detected, and the vacuum level just outside this surface is used as a reference for the other surfaces. From the measurements at the {11$\bar{2}$0} facet a Wz band gap being about 40 meV larger than the Zb was observed, which is in good agreement with our calculated values of 58 meV. In contrast to the theoretically expected type-II alignment, it was observed that the CB edge for both the {110} and the {11$\bar{2}$0} facets was aligned at an n-type state. Due to the alignment and the larger band gap for the Wz InAs, the VB edge for Wz InAs is then placed below the Zb edge, opposite of what is generally believed.[38,39] Interestingly, when adding the local vacuum level (as obtained using PEEM), we note that the electron affinity (CBM to vacuum) of {11$\bar{2}$0} is 30 meV larger than the corresponding value for {110}.

At this point it is worth discussing this discrepancy between theoretically predicted band structure and our measurements in more detail. The theoretical calculations predict changes in the band gap due to changes in the structure very well, while it is the position of the Fermi level that is not given correctly. This can be explained by the difficulty in taking into account the doping of the material which is the result of a variety of defect states both in the bulk and at the surface. For the current NWs, nonintentionally incorporated carbon is the main "bulk" dopant, which indeed leads to n-type doping of the NWs.[48,49] This should already suffice to explain the observed position of the Fermi level in our measurements. However, surface defects are also known to play a very significant role in the doping of NWs, not least for NWs with large surface-to-bulk ratios.[17,50] For defect-free InAs {110} surfaces, no Fermi-level pinning is observed;[51] however in the presence of defects, Fermi-level pinning to the extent of formation of a surface 2DEG has been observed.[21,22,52] Here we point out that all these defects will be clearly observable in STM. In our case we have thus prepared our surfaces with as few defects as possible and recorded spectra as far away from any defects as could be done.

Finally, we use our measurements of electronic structure to interpret previous device measurements. The results from our cleaned NWs—with only minor facet-specific electronic differences—do not explain the dependence of conductivity of Wz and Zb structure in NW devices.[2,8,9] In contrast to the NWs measured here, NWs for device applications have an oxide shell (either native or high-κ), which also affects the electronic properties. In this respect, we note that photoemission spectroscopy (PES) measurements of the effect of oxide removal from NW surfaces[53,54] show that oxide species significantly affect the Fermi level position. Interestingly, depending on the type of NW side facet, varying shifts are observed, thus indicating that the specific type of oxide affects the surface's electronic properties differently. Similar effects have also been observed for InAs planar films.[55,56] Comparing for example the {110} and {10$\bar{1}$0} surfaces, which are unreconstructed and very smooth on the NWs, the change in band alignment due to oxidation is actually very similar, as the oxides are quite similar.[54] However, we observe that the {111}/{$\bar{1}\,\bar{1}\,\bar{1}$}-type surface facets often found on the Zb parts (unless specially tailored as in our case) are quite rough. As a result, these surfaces can have a quite different surface oxide and band alignment.[54] Thus, we conclude that the specific morphology of the crystal facets will be the determining factor for electronic properties, as this can change the oxide interface. Finally we note that, as in a previous study,[17] it will be the oxide close to the crystalline part of the NW that most strongly influences the band alignment, while the outermost part of the oxide and any adsorbates from the air appear less influential. Engineering InAs NW—oxide interfaces that can passivate the surface without affecting the NW electronic properties would thus be highly desirable. Such NWs would also allow for direct modeling and

interpretation of properties using the results presented in this paper.

CONCLUSION

In conclusion we have performed STM, STS, μLEED, PEEM, and *ab initio* calculations on InAs NWs with axial stacking of Wz and Zb segments, deoxidized in an atomic hydrogen atmosphere. Using atomically resolved STM images we have been able to confirm that the most common low-index side facets are unreconstructed, and it was even possible to probe the atomically sharp interface between Wz and Zb parts. Room-temperature STS revealed band gaps of about 350 meV for Zb InAs and about 390 meV for Wz InAs, respectively, qualitatively matching our DFT calculations with the HSE functional. Using surface-sensitive electron microscopy, we have been able to obtain μLEED patterns from Zb and Wz segments as well as mapped out the local vacuum level difference between Wz and Zb InAs, thereby allowing us to determine the most relevant electronic quantities. This is the first successful study of InAs NWs by STS as well as the first report of μLEED patterns obtained from several NW side facets. The findings confirm the larger band gap of Wz InAs compared to Zb InAs, while at the same time demonstrating that the band offsets may be affected by doping even in structurally perfect NWs. Moreover, we find that DFT calculations correctly predict the relative order of band gaps and band offsets and that bulk calculations replicate the STS data close to the band edges, whereas surface calculations need to be considered further away from the band edges. Our results of the band structure and interface charging within the NWs make a solid foundation for understanding InAs NW device behavior since they give a quantitative measure of band offsets and structure, which is a necessity for any reliable interpretation of semiconductor device functionality.[57]

METHODS/EXPERIMENTAL

Single heterostructured InAs NWs with axially stacked Wz and Zb segments were grown by metal−organic vapor phase epitaxy (MOVPE) in an AIXTRON 200/4 system following the particle-assisted growth mode and the use of Au particles. Two different sets of NWs were grown for STM and LEEM/PEEM, respectively. Additional information can be found in the Supporting Information. NWs were grown with axial stacking of Wz−Zb−Wz for the LEEM/PEEM sample and Wz−Zb−Wz−Zb−Wz−Zb for the STM sample. The bottom Wz and Zb segments were mainly terminated by {11$\bar{2}$0}- and {110}-type facets, respectively, resulting from overgrowth in a vapor solid growth mode and thus being grown under identical conditions.[11] The top Wz segments were terminated by {10$\bar{1}$0}-type facets, and the top Zb segment in the STM sample was terminated by alternating {111}/{$\bar{1}\,\bar{1}\,\bar{1}$}-type facets at a twin plane superlattice,[24] as is depicted in Figure 1.

The NWs for STM/S were transferred to an Epi-ready InAs($\bar{1}\,\bar{1}\,\bar{1}$) substrate by mechanical break off and loaded into ultrahigh vacuum (UHV, $p < 10^{-9}$ mbar). Since the NWs were transported in air before the transfer, they were covered by a native oxide, which was removed using a beam of atomic hydrogen at 300−400 °C for 20 min, which has been proven to be a suitable way to remove the native oxide on III−V NWs.[15,16] The cleaned NWs were analyzed in a variable-temperature Omicron XA STM, operated in UHV at room temperature. NWs for LEEM/PEEM were transferred onto a native oxide covered Si(001) and cleaned in a similar fashion to the STM studies. An Elmitec spectroscopic photoemission and low-energy electron microscope (SPELEEM) III operated in UHV at room temperature and connected to the MAX II synchrotron storage ring at the MAX IV laboratory was used. For PEEM, the energy of the X-rays used was between 70 and 600 eV.

For the theoretical determination of the band gap and the band alignment of the InAs polytypes, we performed DFT calculations of bulk Zb, bulk Wz, and combined Zb/Wz supercells. The calculations were performed within the plane-wave approach with the software package VASP.[25] The HSE06 functional[26] was used to describe the electronic exchange and correlation. Additionally, DFT calculations of the InAs NW surfaces were carried out. The side facets of the InAs NWs were modeled by Zb {110} and Wz {11$\bar{2}$0} or {10$\bar{1}$0} surfaces. More information regarding the experiments and theoretical calculations can be found in the Supporting Information.

REFERENCES AND NOTES

1. Dasgupta, N. P.; Sun, J.; Liu, C.; Brittman, S.; Andrews, S. C.; Lim, J.; Gao, H.; Yan, R.; Yang, P. 25th Anniversary Article: Semiconductor Nanowires—Synthesis, Characterization, and Applications. *Adv. Mater.* **2014**, *26*, 2137–2184.

2. Thelander, C.; Caroff, P.; Plissard, S.; Dey, A. W.; Dick, K. A. Effects of Crystal Phase Mixing on the Electrical Properties of InAs Nanowires. *Nano Lett.* **2011**, *11*, 2424–2429.

3. Wei, W.; Bao, X.-Y.; Soci, C.; Ding, Y.; Wang, Z.-L.; Wang, D. Direct Heteroepitaxy of Vertical InAs Nanowires on Si Substrates for Broad Band Photovoltaics and Photodetection. *Nano Lett.* **2009**, *9*, 2926–2934.

4. Egard, M.; Johansson, S.; Johansson, A. C.; Persson, K. M.; Dey, A. W.; Borg, B. M.; Thelander, C.; Wernersson, L. E.; Lind, E. Vertical InAs Nanowire Wrap Gate Transistors with $f_t > 7$ GHz and $f_{max} > 20$ GHz. *Nano Lett.* **2010**, *10*, 809–812.

5. Bjork, M. T.; Schmid, H.; Bessire, C. D.; Moselund, K. E.; Ghoneim, H.; Karg, S.; Lortscher, E.; Riel, H. Si−InAs Heterojunction Esaki Tunnel Diodes with High Current Densities. *Appl. Phys. Lett.* **2010**, *97*, 163501–3.

6. Chuang, S.; Gao, Q.; Kapadia, R.; Ford, A. C.; Guo, J.; Javey, A. Ballistic InAs Nanowire Transistors. *Nano Lett.* **2012**, *13*, 555–558.

7. Das, A.; Ronen, Y.; Most, Y.; Oreg, Y.; Heiblum, M.; Shtrikman, H. Zero-Bias Peaks and Splitting in an Al-InAs Nanowire Topological Superconductor as a Signature of Majorana Fermions. *Nat. Phys.* **2012**, *8*, 887–895.

8. Schroer, M. D.; Petta, J. R. Correlating the Nanostructure and Electronic Properties of InAs Nanowires. *Nano Lett.* **2010**, *10*, 1618–1622.

9. Dayeh, S. A.; Susac, D.; Kavanagh, K. L.; Yu, E. T.; Wang, D. Structural and Room-Temperature Transport Properties of Zinc Blende and Wurtzite InAs Nanowires. *Adv. Funct. Mater.* **2009**, *19*, 2102–2108.

10. Dick, K. A.; Bolinsson, J.; Messing, M. E.; Lehmann, S.; Johansson, J.; Caroff, P. Parameter Space Mapping of InAs Nanowire Crystal Structure. *J. Vac. Sci. Technol. B* **2011**, *29*, 04D103.

11. Lehmann, S.; Wallentin, J.; Jacobsson, D.; Deppert, K.; Dick, K. A. A General Approach for Sharp Crystal Phase Switching in InAs, GaAs, InP, and GaP Nanowires Using Only Group V Flow. *Nano Lett.* **2013**, *13*, 4099–4105.

12. Yu, E. T. Cross-Sectional Scanning Tunneling Microscopy. *Chem. Rev.* **1997**, *97*, 1017–1044.

13. Capiod, P.; Xu, T.; Nys, J. P.; Berthe, M.; Patriarche, G.; Lymperakis, L.; Neugebauer, J.; Caroff, P.; Dunin-Borkowski, R. E.; Ebert, P.; Grandidier, B. Band Offsets at Zincblende-Wurtzite GaAs Nanowire Sidewall Surfaces. *Appl. Phys. Lett.* **2013**, *103*, 122104–4.

14. Xu, T.; Dick, K. A.; Plissard, S.; Nguyen, T. H.; Makoudi, Y.; Berthe, M.; Nys, J. P.; Wallart, X.; Grandidier, B.; Caroff, P. Faceting, Composition and Crystal Phase Evolution in III-V Antimonide Nanowire Heterostructures Revealed by Combining Microscopy Techniques. *Nanotechnology* **2012**, *23*, 095702.

15. Hjort, M.; Lehmann, S.; Knutsson, J.; Timm, R.; Jacobsson, D.; Lundgren, E.; Dick, K. A.; Mikkelsen, A. Direct Imaging of Atomic Scale Structure and Electronic Properties of GaAs Wurtzite and Zinc Blende Nanowire Surfaces. *Nano Lett.* **2013**, *13*, 4492–4498.

16. Hilner, E.; Hakanson, U.; Froberg, L. E.; Karlsson, M.; Kratzer, P.; Lundgren, E.; Samuelson, L.; Mikkelsen, A. Direct Atomic Scale Imaging of III-V Nanowire Surfaces. *Nano Lett.* **2008**, *8*, 3978–3982.

17. Hjort, M.; Wallentin, J.; Timm, R.; Zakharov, A. A.; Håkanson, U.; Andersen, J. N.; Lundgren, E.; Samuelson, L.; Borgström, M. T.; Mikkelsen, A. Surface Chemistry, Structure, and Electronic Properties from Microns to the Atomic Scale of Axially Doped Semiconductor Nanowires. *ACS Nano* **2012**, *6*, 9679.

18. Hjort, M.; Wallentin, J.; Timm, R.; Zakharov, A. A.; Andersen, J. N.; Samuelson, L.; Borgstrom, M. T.; Mikkelsen, A. Doping Profile of InP Nanowires Directly Imaged by Photoemission Electron Microscopy. *Appl. Phys. Lett.* **2011**, *99*.

19. Zakharov, A. A.; Mikkelsen, A.; Andersen, J. N. Recent Advances in Imaging of Properties and Growth of Low Dimensional Structures for Photonics and Electronics by XPEEM. *J. Electron Spectrosc.* **2012**, *185*, 417–428.

20. Kronik, L.; Shapira, Y. Surface Photovoltage Phenomena: Theory, Experiment, and Applications. *Surf. Sci. Rep.* **1999**, *37*, 1–206.

21. Weber, J. R.; Janotti, A.; Van de Walle, C. G. Intrinsic and Extrinsic Causes of Electron Accumulation Layers on InAs Surfaces. *Appl. Phys. Lett.* **2010**, *97*, 192106–3.

22. Olsson, L. Ö.; Andersson, C. B. M.; Håkansson, M. C.; Kanski, J.; Ilver, L.; Karlsson, U. O. Charge Accumulation at InAs Surfaces. *Phys. Rev. Lett.* **1996**, *76*, 3626–3629.

23. Du, Y. A.; Sakong, S.; Kratzer, P. As Vacancies, Ga Antisites, and Au Impurities in Zinc Blende and Wurtzite GaAs Nanowire Segments from First Principles. *Phys. Rev. B* **2013**, *87*, 075308.

24. Algra, R. E.; Verheijen, M. A.; Borgström, M. T.; Feiner, L. F.; Immink, G.; van Enckevort, W. J. P.; Vlieg, E.; Bakkers, E. P. A. M. Twinning Superlattices in Indium Phosphide Nanowires. *Nature* **2008**, *456*, 369–372.

25. Kresse, G.; Furthmüller, J. Efficient Iterative Schemes for ab Initio Total-Energy Calculations Using a Plane-Wave Basis Set. *Phys. Rev. B* **1996**, *54*, 11169–11186.

26. Heyd, J.; Scuseria, G. E.; Ernzerhof, M. Hybrid Functionals Based on a Screened Coulomb Potential. *J. Chem. Phys.* **2003**, *118*, 8207–8215.

27. Kawaguchi, K.; Heurlin, M.; Lindgren, D.; Borgstrom, M. T.; Ek, M.; Samuelson, L. InAs Quantum Dots and Quantum Wells Grown on Stacking-Fault Controlled InP Nanowires with Wurtzite Crystal Structure. *Appl. Phys. Lett.* **2011**, *99*, 131915–3.

28. Knutsson, J.; Lehmann, S.; Hjort, M.; Reinke, P.; Lundgren, E.; Dick, K. A.; Timm, R.; Mikkelsen, A. Atomic Scale Surface Structure and Morphology of InAs Nanowire Crystal Superlattices: The Effect of Epitaxial Overgrowth. *ACS Appl. Mater. Interfaces* **2014**, submitted.

29. Belabbes, A.; Furthmüller, J.; Bechstedt, F. Relation between Spontaneous Polarization and Crystal Field from First Principles. *Phys. Rev. B* **2013**, *87*, 035305.

30. Gaan, S.; Feenstra, R. M.; Ebert, P.; Dunin-Borkowski, R. E.; Walker, J.; Towe, E. Structure and Electronic Spectroscopy of Steps on GaAs(110) Surfaces. *Surf. Sci.* **2012**, *606*, 28–33.

31. Heinrich, M.; Domke, C.; Ebert, P.; Urban, K. Charged Steps on III-V Compound Semiconductor Surfaces. *Phys. Rev. B* **1996**, *53*, 10894–10897.

32. Feenstra, R. M.; Lee, J. Y.; Kang, M. H.; Meyer, G.; Rieder, K. H. Band Gap of the Ge(111)c(2×8) Surface by Scanning Tunneling Spectroscopy. *Phys. Rev. B* **2006**, *73*, 035310.

33. Ma, D. D. D.; Lee, C. S.; Au, F. C. K.; Tong, S. Y.; Lee, S. T. Small-Diameter Silicon Nanowire Surfaces. *Science* **2003**, *299*, 1874–1877.

34. Feenstra, R. M.; Dong, Y.; Semtsiv, M. P.; Masselink, W. T. Influence of Tip-Induced Band Bending on Tunnelling Spectra of Semiconductor Surfaces. *Nanotechnology* **2007**, *18*, 044015.

35. Timm, R.; Feenstra, R. M.; Eisele, H.; Lenz, A.; Ivanova, L.; Lenz, E.; Dahne, M. Contrast Mechanisms in Cross-Sectional Scanning Tunneling Microscopy of GaSb/GaAs Type-II Nanostructures. *J. Appl. Phys.* **2009**, *105*, 093718.

36. SEMITIP software; http://www.andrew.cmu.edu/user/feenstra/semitip_v6/.

37. Feenstra, R. M.; Stroscio, J. A. Tunneling Spectroscopy of the Gaas(110) Surface. *J. Vac. Sci. Technol. B* **1987**, *5*, 923–929.

38. Murayama, M.; Nakayama, T. Chemical Trend of Band Offsets at Wurtzite/Zinc-Blende Heterocrystalline Semiconductor Interfaces. *Phys. Rev. B* **1994**, *49*, 4710–4724.

39. Belabbes, A.; Panse, C.; Furthmüller, J.; Bechstedt, F. Electronic Bands of III-V Semiconductor Polytypes and their Alignment. *Phys. Rev. B* **2012**, *86*, 075208.

40. Tragardh, J.; Persson, A. I.; Wagner, J. B.; Hessman, D.; Samuelson, L. Measurements of the Band Gap of Wurtzite InAs$_{1-x}$P$_x$ Nanowires Using Photocurrent Spectroscopy. *J. Appl. Phys.* **2007**, *101*, 123701–4.

41. De, A.; Pryor, C. E. Predicted Band Structures of III-V Semiconductors in the Wurtzite Phase. *Phys. Rev. B* **2010**, *81*, 155210.

42. Noguchi, M.; Hirakawa, K.; Ikoma, T. Intrinsic Electron Accumulation Layers on Reconstructed Clean InAs(100) Surfaces. *Phys. Rev. Lett.* **1991**, *66*, 2243–2246.

43. Wirths, S.; Weis, K.; Winden, A.; Sladek, K.; Volk, C.; Alagha, S.; Weirich, T. E.; von der Ahe, M.; Hardtdegen, H.; Lüth, H.; Demarina, N.; Grützmacher, D.; Schäpers, T. Effect of Si-Doping on InAs Nanowire Transport and Morphology. *J. Appl. Phys.* **2011**, *110*, 053709.

44. Feenstra, R. M. Tunneling Spectroscopy of the (110)-Surface of Direct-Gap III-V Semiconductors. *Phys. Rev. B* **1994**, *50*, 4561–4570.

45. Jona, F.; J. A. Strozier, J.; Yang, W. S. Low-Energy Electron Diffraction for Surface Structure Analysis. *Rep. Prog. Phys.* **1982**, *45*, 527.

46. Cahen, D.; Kahn, A. Electron Energetics at Surfaces and Interfaces: Concepts and Experiments. *Adv. Mater.* **2003**, *15*, 271–277.

47. Renault, O.; Brochier, R.; Roule, A.; Haumesser, P. H.; Krömker, b.; Funnemann, D. Work-Function Imaging of Oriented Copper Grains by Photoemission. *Surf. Interface Anal.* **2006**, *38*, 375–377.

48. Fang, Z. M.; Ma, K. Y.; Cohen, R. M.; Stringfellow, G. B. Effect of Growth Temperature on Photoluminescence of InAs Grown by Organometallic Vapor Phase Epitaxy. *Appl. Phys. Lett.* **1991**, *59*, 1446–1448.

49. Thelander, C.; Dick, K. A.; Borgstrom, M. T.; Froberg, L. E.; Caroff, P.; Nilsson, H. A.; Samuelson, L. The Electrical and Structural Properties of n-Type InAs Nanowires Grown from Metal-Organic Precursors. *Nanotechnology* **2010**, *21*, 205703.

50. Ford, A. C.; Ho, J. C.; Chueh, Y.-L.; Tseng, Y.-C.; Fan, Z.; Guo, J.; Bokor, J.; Javey, A. Diameter-Dependent Electron Mobility of InAs Nanowires. *Nano Lett.* **2008**, *9*, 360–365.

51. Wildöer, J. W. G.; Harmans, C. J. P. M.; van Kempen, H. Observation of Landau Levels at the InAs(110) Surface by Scanning Tunneling Spectroscopy. *Phys. Rev. B* **1997**, *55*, R16013–R16016.

52. Castleton, C. W. M.; Höglund, A.; Göthelid, M.; Qian, M. C.; Mirbt, S. Hydrogen on III-V (110) Surfaces: Charge Accumulation and STM Signatures. *Phys. Rev. B* **2013**, *88*, 045319.

53. Timm, R.; Hjort, M.; Fian, A.; Thelander, C.; Lind, E.; Andersen, J. N.; Wernersson, L. E.; Mikkelsen, A. Interface Composition of Atomic Layer Deposited HfO_2 and Al_2O_3 Thin Films on InAs Studied by X-Ray Photoemission Spectroscopy. *Microelectron. Eng.* **2011**, *88*, 1091–1094.

54. Timm, R. Manuscript in preparation.

55. Tsui, D. C. Observation of Surface Bound State and Two-Dimensional Energy Band by Electron Tunneling. *Phys. Rev. Lett.* **1970**, *24*, 303–306.

56. Baier, H. U.; Koenders, L.; Mönch, W. Oxidation of InAs(110) and Correlated Changes of Electronic Surface Properties. *J. Vac. Sci. Technol. B* **1986**, *4*, 1095–1099.

57. Kroemer, H. Nobel Lecture: Quasielectric Fields and Band Offsets: Teaching Electrons New Tricks. *Rev. Mod. Phys.* **2001**, *73*, 783–793.